[5] H. Sirringhaus, P. J. Brown, R. H. Friend, M. M. Nielsen, K. Bechgaard, B. M. W. Langeveld-Voss, A. J. H. Spiering, R. A. J. Janssen, E. W. Meijer, P. T. Herwig, D. M. de Leeuw, *Nature* **1999**, *401*, 685.
[6] H. Sirringhaus, T. Kawase, R. H. Friend, T. Shimoda, M. Inbasekaran, W. Wu, E. P. Woo, *Science* **2000**, *290*, 2123.
[7] C. J. Drury, C. M. J. Mutsaers, C. M. Hart, M. Matters, D. M. d. Leeuw, *Appl. Phys. Lett.* **1998**, *73*, 108.
[8] F. Garnier, R. Hadjlaoui, A. Yasser, P. Srivastava, *Science* **1994**, *265*, 1684.
[9] J. A. Rogers, Z. Bao, V. R. Raju, *Appl. Phys. Lett.* **1998**, *72*, 2716.
[10] C. Gray, J. Wang, G. Duthaler, A. Ritenour, P. S. Drzaic, *Proc. SPIE-Int. Soc. Opt. Eng.* **2001**, *4466*, 89.
[11] T. R. Hebner, C. C. Wu, D. Marcy, M. H. Lu, J. C. Sturm, *Appl. Phys. Lett.* **1998**, *72*, 519.
[12] S.-C. Chang, J. Liu, J. Bharathan, Y. Yang, *Adv. Mater.* **1999,** *11*, 734.
[13] E. I Haskal, M. Büchel, P. C. Duineveld, A. Sempel, P. van de Weijer, *Mater. Res. Soc. Bull.* **2002**, *27*, 864.
[14] S. P. Speakman, G. G. Rozenberg, K. J. Clay, W. I. Milne, A. Ille, I. A. Gardner, E. Bresler, J. H. G. Steinke, *Org. Electron.* **2001**, *2*, 65.
[15] K. E. Paul, W. S. Wong, S. Ready, R. A. Street, *Appl. Phys. Lett.* **2003**, *83*, 2070.
[16] W. S. Wong, S. E. Ready, J.-P. Lu, R. A. Street, *IEEE Electron Device Lett.* **2003**, *24*, 577.
[17] B. S. Ong, P. Liu, Y. Wu, unpublished.
[18] H. Sirringhaus, R. J. Wilson, R. H. Friend, M. Inbasekaran, W. Wu, E. P. Woo, M. Grell, D. D. C. Bradley, *Appl. Phys. Lett.* **2000**, *77*, 406.
[19] D. Myers, *Surfaces, Interfaces, and Colloids*, Wiley-VCH, New York **1999**.
[20] E. Kim, Y. Xia, G. M. Whitesides, *Nature* **1995**, *376*, 581.
[21] E. Kim, G. M. Whitesides, *J. Phys. Chem. B* **1997**, *101*, 855.
[22] R. R. Rye, J. J. A. Mann, F. G. Yost, *Langmuir* **1996**, *12*, 555.
[23] A. A. Darhuber, S. M. Troian, W. W. Reisner, *Phys. Rev. E* **2001**, *64*, 031603–1.
[24] R. A. Street, A. Salleo, M. L. Chabinyc, *Phys. Rev. B* **2003**, *68*, 085 316.
[25] A. Salleo, M. L. Chabinyc, M. S. Yang, R. A. Street, *Appl. Phys. Lett.* **2002**, *81*, 4383.
[26] J. Hu, R. G. Beck, T. Deng, R. M. Westervelt, K. D. Maranowski, A. C. Gossard, G. M. Whitesides, *Appl. Phys. Lett.* **1997**, *71*, 2020.

ZnO Nanoribbon Microcavity Lasers**

By *Haoquan Yan*, *Justin Johnson*, *Matt Law*, *Rongrui He*, *Kelly Knutsen*, *Juan R. McKinney*, *Johnny Pham*, *Richard Saykally*,* and *Peidong Yang**

Exploration of one-dimensional semiconductor nanostructures has led to great progress in the areas of optoelectronics in the past few years.[1] Nanolasers,[2–4] waveguides,[5] frequency converters (second or third harmonic generators),[6] photoconductive optical switches,[7] and sensors[8,9] have been developed based on oxide nanowires. The single crystalline nature of these nanowires makes them ideal candidates for probing size-dependent and dimensionality-controlled physical phenomena. In particular, the transverse nanoscale and longitudinal microscale dimensions (i.e., large aspect ratio) as well as well-defined faceting nature of such nanostructures enable the observation of unique optical confinement and microcavity effects.[2–4] Previously, hexagonal cylindrical ZnO nanowires have been examined as a laser gain medium.[2–4] These nanocylinders indeed can serve as miniaturized Fabry–Perot optical cavities in the ultraviolet (UV) region with high gain and quality factor.[10] Based on classical waveguide theory, different transverse optical modes can be sustained within waveguides of different cross-sections.[11] It is thus fundamentally interesting to examine the optical cavity effects within nanowires with cross-sections other than hexagonal. Herein, we examine the lasing phenomenon from ZnO nanoribbons with pseudo-rectangular cross-section. Cavity-length dependent optical mode analysis reveals different cavity effects from those of hexagonal nanocylinders.

ZnO, being environmentally benign and having a large bandgap (3.37 eV) and exciton binding energy (60 meV), has been considered as a promising candidate for UV light-emitting diodes and laser diodes. It has also displayed an astonishing series of nanostructures with different morphologies.[12] Among many others, the hexagonal nanocylinders,[2–4] nanoribbons,[5,13] tetrapods,[12] and comb-like nanowire arrays[14] are highly interesting for their fundamental significance in revealing microcavity effects as well as near-field optical coupling phenomena.

The ZnO nanoribbons in this work were synthesized using two methodologies. One is a carbon thermal reduction process at 900 °C.[12] The other is the high temperature (1350 °C) approach developed by Wang and co-workers.[13] The two methods involve different growth mechanisms. The low temperature process utilized Au as the growth initiator. The observation of Au nanoparticles on the nanoribbon tips in the transmission electron microscope (TEM, Figure 1B) suggests that this is a vapor–liquid–solid (VLS) growth process. In contrast, the high-temperature approach is a vapor–solid (VS) growth process without any foreign metal initiation. Regardless of these different growth mechanisms, the growth directions and side facets of the produced nanoribbons are identical for the two sets of the samples. The length of the ribbons is about 10–60 μm, the width is about 0.1–1 μm, and the thickness is about 10–200 nm (Fig. 1). Electron diffraction (Fig. 1B inset), cross-sectional scanning electron microscopy (SEM, Figure 1A inset), and TEM characterization show that these nanoribbons are single crystalline; they grow along the $[01\bar{1}0]$ direction, are enclosed by $\pm(2\bar{1}\bar{1}0)$ and $\pm(0001)$ facets, and hence possess pseudo-rectangular cross-sections. Some of them have the $\pm(2\bar{1}\bar{1}0)$ facets as the wide surfaces and the $\pm(0001)$ facets as the narrow surfaces (Fig. 1B), while the other ones have the $\pm(0001)$ facets as the wide side-planes and the $\pm(2\bar{1}\bar{1}0)$ facets as the narrow side-planes (Fig. 1C). Importantly, the observation of Au nanoparticles at the tips of the ZnO nanoribbons is strong evidence that these ZnO nanoribbons can indeed be grown via the VLS mechanism at relatively low temperature.

To explore the optical properties of single ZnO nanoribbons, the ribbons were removed from the growth substrate by

[*] Prof. P. Yang, Prof. R. Saykally, H. Yan, J. Johnson, M. Law, R. He, K. Knutsen, J. R. McKinney, J. Pham
Department of Chemistry
Lawrence Berkeley National Laboratory
University of California, Berkeley, CA 94720
Email: p_yang@uclink.berkeley.edu, saykally@uclink.berkeley.edu

[**] This work was supported by the Camille and Henry Dreyfus Foundation, Beckman Foundation, the National Science Foundation and Department of Energy. P. Y. is an Alfred P. Sloan Research Fellow. Work at the Lawrence Berkeley National Laboratory was supported by the Office of Science, Basic Energy Sciences, Division of Materials Science of the U.S. Department of Energy. We thank the National Center for Electron Microscopy for the use of their facilities. H. Yan and J. Johnson contributed equally to this work.

ADVANCED MATERIALS

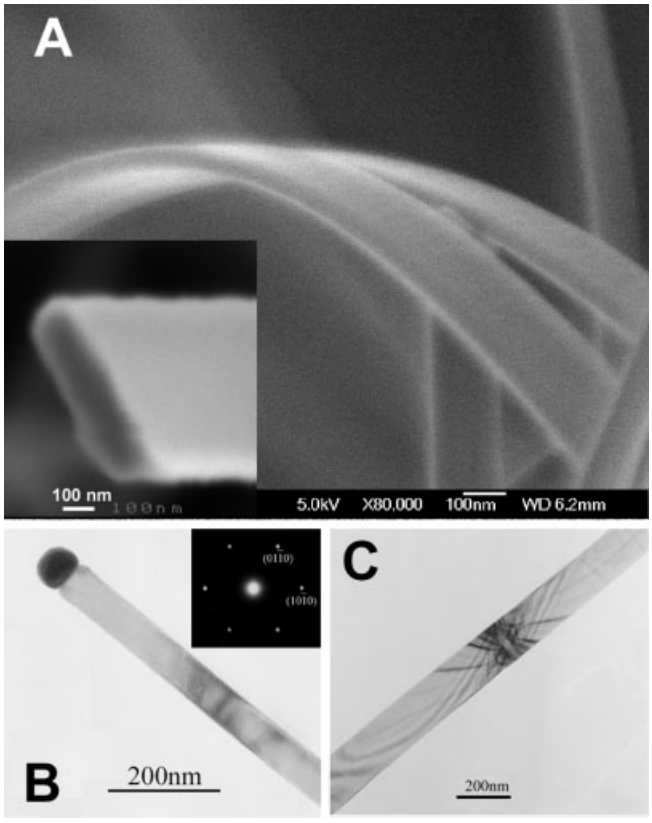

Fig. 1. SEM and TEM images of the ZnO nanoribbons. A) Low magnification SEM image; inset shows a cross-section of a nanoribbon. B,C) TEM images of the ZnO nanoribbons grown at 900 and 1400 °C, respectively. Inset shows selective area diffraction (SAD) pattern from the ribbon shown in (B).

ultrasonication and dispersed onto a sapphire substrate by drop-casting an isoproponal–nanoribbon suspension. These well-dispersed ribbons were imaged by a far-field imaging system using a femtosecond laser as the excitation source. Figure 2 shows a typical far-field photoluminescence (PL) image and the spectra collected on a single nanoribbon with the length about 15 μm, and cross-section of 1 μm × 200 nm. As shown in the far-field image, strong emission was observed from both ends of the ribbon and almost no signal can be detected from the side surfaces. This is a clear indication of waveguiding of UV emission by the nanoribbon itself. A general signature of the power-dependent emission is as follows. With the increase of excitation power, significant peak narrowing was observed with superlinear emission intensity increase, which suggests a transition from spontaneous emission to stimulated emission. The line width of many of these cavity modes appears to be in the range of 0.1–0.5 nm, suggesting microcavities with quality factor $\sim 3 \times 10^3$ (The quality factor of a resonant system is a measure of how "sharp" a resonance is). The finesse can also be estimated to be 1.6 based on the end facet reflectivity (0.18). As shown in Figure 2B, with further increase in excitation power, more cavity modes (both transverse and longitudinal ones) would emerge as a result of broadened gain profiles. We note here that highly nonlinear gain combimed with distinct cavity modes at the quoted pump

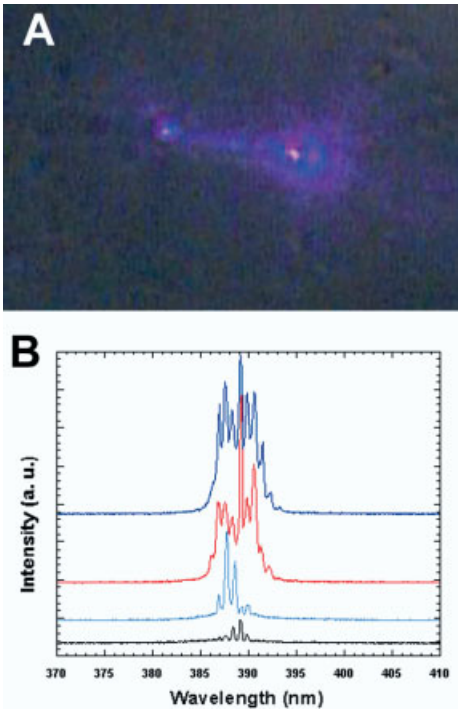

Fig. 2. A) Photoluminescence image of a single ZnO nanoribbon dispersed on a sapphire substrate. The ribbon was pumped by a femtosecond laser with pulse width about 200 fs and pumping wavelength of 310 nm. B) The emission spectra collected at different pump intensity. From bottom up, the pump fluence (intensity) is 1.0, 1.05, 1.1, and 1.25 μJ cm^{-2}.

fluences is a clear indication of the lasing process.[2,3,10] We have observed passive resonator modes in nanostructures of other materials, in which gain is minimal (tin dioxide, for example), and there is an obvious distinction between the behaviors in the passive and active media. The sharp threshold accompanying the lasing behavior clearly distinguishes it from passive PL waveguiding.

The nanoribbon geometry resembles many microfabricated laser structures based on strip or slab waveguide geometry. Either single-transverse mode or multiple modes can be sustained within such microcavities depending on the dimension of the structures. Based upon classical waveguide theory,[11,15] single-mode operation (TE_0, TM_0) occurs for an infinite symmetric planar waveguide with a thickness less than 90 nm. The number of guided modes increases roughly proportional to the thickness of the planar waveguide. Thus, one would expect a complicated set of transverse modes as the waveguide thickness increases. Hexagonal (or near-circular) cross-section wires have similar mode structure (the first few of them being HE_{11}, TE_{01}, TM_{01}), with the radius being the critical dimension.[10,16] However, the axial symmetry of wires is not present in the ribbons with rectangular cross-sections. The exact transverse mode structures (collections of TE_{mn} and TM_{mn} modes) will be more complicated and also depend on the ribbon width/thickness. Preliminary simulation indicates that the nanoribbon can sustain single mode when the thickness of the ribbon is about 60–80 nm, and similarly more modes for thicker nanoribbons.

The spacing of the longitudinal modes that accompany each transverse mode depends critically on the effective path length of the mode, which for Fabry–Perot resonators would simply be the ribbon length. However, since high reflectivity exists in both axial and transverse directions (with respect to the long axis of the ribbon), one would not expect that all modes would be of the pure axial Fabry–Perot type, but instead some of them might contain significant non-axial wave vector. For example, these "bow-tie" shaped modes have been clearly identified in a layered semiconductor microcavities.[17] The existence of these "bow-tie" modes is expected to narrow the effective mode spacing and modify the directional emission properties.

For certain nanoribbons, we were able to distinguish different sets of transverse modes when we increased the pump intensity. Figure 3A shows a far-field emission image of another nanoribbon with ~550 nm × 110 nm × 35 μm (width × thickness × length). The power dependent (Fig. 3B) study indicates a lasing threshold of 3.2 μJ cm^{-2} for this single ribbon. If we assume these nanoribbons serve as Farby–Perot optical cavities like their hexagonal nanocylinder counterparts, the longitudinal modes spacing is expected to be determined by the equation below:

$$\Delta\lambda = \frac{\lambda^2}{2nL} \quad (1)$$

where n is the group refractive index and L is the effective cavity length. For a ZnO nanoribbon with length about 35 μm, the mode spacing for the longitudinal modes is expected to be ~0.85 nm. This is consistent with what we observed just above the lasing threshold, where the observed mode spacing is about 0.8 nm (Fig. 3C lower curve). We believe this set of longitudinal modes is associated with the fundamental transverse mode supported within the nanoribbon cavity. As the nanoribbon has a fairly large cross-section, it can support additional transverse modes. Consequently, when the excitation power is increased, the gain profiles can be broadened so that higher-order modes would emerge. As shown in Figure 3C (upper curve), another set of transverse modes appears in the spectrum. The mode spacing for this set of peaks also agrees well with the Fabry–Perot cavity assumption. Note, however, there is a blue shift for this higher mode when compared with lower order transverse modes. At this point, the exact relationship between these different transverse modes is not clear, nor the evolution of gain profiles as we increase the pump intensity. We note that for most nanoribbons, the lasing thresholds are higher than those of nanowires,[2,3,10,18] which could be a result of the completely different geometry and end facet quality.

In order to gain in-depth understanding of the lasing phenomenon in these nanoribbon microcavities, we carried out length-dependent lasing studies on single nanoribbons. Focused ion beam (FIB) etching was used to obtain different ribbon lengths.[19–21] FIB etching is ideal for this purpose in order to uniformly reduce the ribbon length by known increments without significantly affecting the quality of the ribbon cavity.

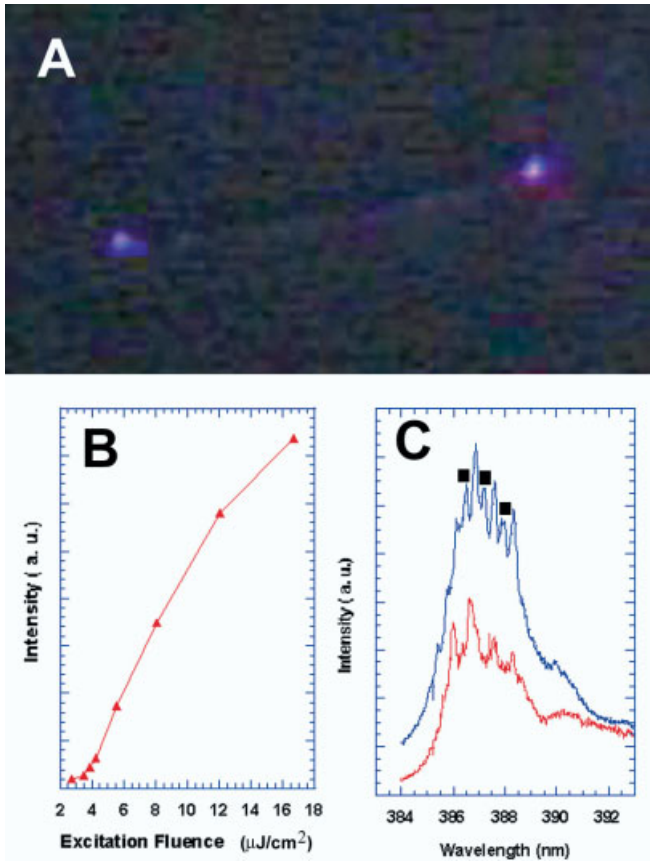

Fig. 3. A) Photoluminescence far-field image of a single ZnO nanoribbon dispersed on a sapphire substrate. B) Power-dependent integrated emission intensity on this ZnO nanoribbon. C) Emission spectra taken on the ribbon at two excitation powers above the lasing threshold (5.5 and 6.8 μJ cm^{-2}). The second set of transverse modes is marked as "■".

Between etches, the individual ribbons are studied optically to characterize their lasing thresholds and the mode spacings.

The results of these length-dependent lasing studies on ZnO nanoribbons are shown in Figure 4. As shown in Figure 4A, the FIB etched through the ribbon in a well-defined region at the desired position, with surface roughness to be less than 100 nm. The potential issue of end facet erosion was minimized by confining the ion beam to a small region (< 200 nm) at the end of the ribbon. With this method, Ga^+ ion implantation can be effectively avoided, and the change in length of the ribbon is not significant enough to affect the lasing threshold. Several such etches were performed, and no change in the lasing threshold was observed within the experimental uncertainty (5 % change). It is interesting that the end facet distortion that appears after some etches does not significantly affect the lasing threshold or spectrum, which suggests that the etched ribbons could lase via a morphology-dependent or "bow-tie" resonance. In any case, it appears as though controlled etching in this manner sidesteps any detrimental effects of FIB etching on the optical waveguide properties.

Series of lasing spectra from a single ribbon were collected at several ribbon lengths. One clear trend is that the mode spacing increases with decreasing nanoribbon length

ADVANCED MATERIALS

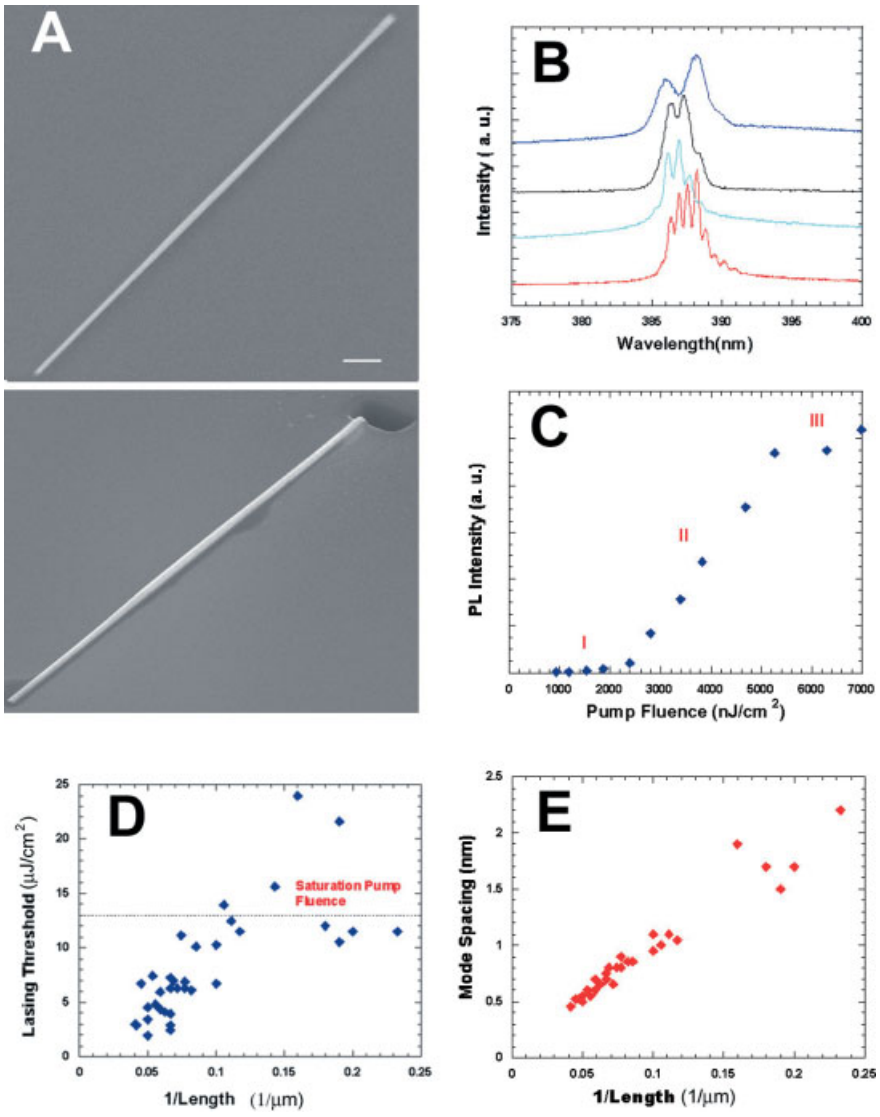

Fig. 4. A) SEM images demonstrating the successive FIB etching method on single ZnO ribbons. The images were captured at constant magnification and field of view after 30 s of 30 keV gallium ion beam irradiation. Scale bar = 2 μm. The etching also results in a depression in the Si substrate, as can be seen in the images. B) Series of lasing spectra from a single ribbon taken at several ribbon lengths (from bottom up, 18, 13, 10, 4.5 μm). C) Pump fluence dependence of the overall lasing intensity for a typical ribbon laser showing the saturation region. D) Length dependence of the lasing threshold. E) Dependence of the spectral mode spacing on the length of the ribbon. Mode spacing is measured without deconvolution of multiple transverse modes.

(Fig. 4B). The data in Figures 4D,E are a compilation taken from six separate structures. The lasing threshold shows an approximately linear increase with the reciprocal length for lengths down to 7 μm. This behavior is expected, considering the dependence of the lasing threshold on the gain and length of the nanowire. The threshold can be determined by considering the condition for lasing (i.e., round-trip loss equals gain),

$$g_{th} = \alpha + 1/2\, L \ln[R_1 R_2] \quad (2)$$

where R is the end facet reflection and α is the loss along the ribbon length. The α term is expected to be minimally affected by the etching and will be considered as a constant. Also, the reflection losses are expected to dominate the overall loss term since the reflectivity for normal incidence at the ZnO–air interface is only about 0.19.[16] The gain coefficient for the ribbon depends directly on the population inversion within the lattice, which monotonically increases with pumping intensity above the lasing threshold in the region of stimulated emission. However, this inversion saturates at high pumping intensities, as is shown in Figure 4C (region III). With an incremental decrease in the ribbon length, the gain must be increased by a similar amount in order for the lasing threshold to be reached. This additional gain is provided by pumping the ribbon with higher intensity in order to increase the material inversion. As a result, the threshold pump fluence and the ribbon length are inversely proportional (Fig. 4D). In region III (Fig. 4C), the gain is pinned, and thus increased pumping intensity cannot compensate for the loss of ribbon length. Therefore, most ribbons with $L < 6$ μm cannot support lasing.

In some cases, ribbons with very low losses can support lasing with $L < 5$ μm (Fig. 4D). The thresholds in this regime, however, no longer follow the $1/L$ dependence and instead show a nearly constant dependence on length. This is possibly due to a change in the lasing characteristics that accompanies the altered aspect ratio after FIB etching. When primarily axial modes may not experience sufficient gain to sustain lasing, "bow-tie" modes with large transverse wavevector and larger effective cavity lengths could dominate. This effect is also observed in the lasing spectrum, as the mode spacing for $L < 5$ μm does not follow the typical $1/L$ dependence that is observed for single set of transverse modes when $L > 10$ μm (Figs. 4E). The geometry of these short ribbons brings the structure to a distinct regime from that studied with typical 1D structures, and further investigation of the nature of lasing in this regime is required for a better understanding of the underlying optical physics.

In summary, ZnO nanoribbons with pseudo-rectangular cross-sections were demonstrated here as excellent microcavities with a high quality factor (~3000). The length-dependent lasing threshold studies were carried out on single ribbon structures using a novel FIB etching method. It is found that the lasing threshold is inversely proportional to the length of

the ribbon before the pumping intensity reaches the saturation region. Analysis of the emission points to the possibility of the existence of both pure axial modes and "bow-tie" cavity modes depending on the length of the nanoribbon cavity.

Experimental

ZnO nanoribbons are synthesized using a ZnO/C (1:1) mixture as the Zn vapor source. The substrates were coated with 20 Å Au, and they were put on top of the alumina boat, which is located at the center of a quartz tube in a tube furnace. Pure argon was used as the carrier gas at about 10 sccm (standard cubic centimeters per minute). The reaction was carried out at 900 °C for 10 min. Normally, after the reaction the substrate was coated with a layer of gray powder. The thickness of the gray coating is generally about 5–10 μm. For the high temperature approach, ZnO powder was heated to 1350 °C in a flow of argon at 300 torr in an alumina tube. The single-crystalline ZnO ribbons were collected on ceramic Al_2O_3 substrates, suspended in the isoproponal solution by ultrasonication and then dispersed onto Si (100) substrates for optical measurements. The crystal structures were analyzed using X-ray diffraction (XRD, Siemens D5000 apparatus). Morphology and size distribution of the crystals were characterized using SEM (JOEL6400 or JSM-6430 apparatus operated at 5 keV). TEM studies of the crystals were carried out on Philips CM200 apparatus operated at 200 keV.

Individual nanoribbons were sputter-etched in a FEI xPDB FIB/SEM system with a 1000 pA gallium ion beam at 30 keV. A typical etch took 10–20 s. Care was taken to minimize sample exposure to the ion beam by searching and imaging in electron beam mode.

The optical measurements were performed using regeneratively amplified pulses from a homebuilt Ti:sapphire oscillator. The pulses were converted using a commercial optical parametric amplifier (OPA, Quantronix, TOPAS apparatus), resulting in ~ 200 fs pulses at 310 nm. The excitation laser was focused on the sample obliquely (spot size ~ 100 μm × 200 μm), and single nanoribbons were identified using a homebuilt microscope with 500–1000 nm resolution. The PL and lasing light were collected using an objective (numerical aperture 0.7), coupled into an optical fiber, and dispersed onto a liquid nitrogen cooled charge coupled device (CCD) with a 0.3 m spectrograph, while the scattered light was filtered. Typical spectral resolution was 0.1 nm, although a 0.5 m spectrograph (0.05 nm resolution) was also used to test the narrowest spectral features.

The lasing threshold measurement was internally calibrated (i.e., a reference was used to normalize all of the data presented in Fig. 4D) so that variations in pumping intensity and geometry after successive etchings would not contribute to the trend. Analysis of the modes in the lasing spectrum was done consistently near 385 nm after each etch, in order to avoid dispersion effects.

Received: June 3, 2003
Final version: August 20, 2003
Published online: October 16, 2003

[1] Y. Xia, P. Yang, Y. Sun, Y. Wu, B. Mayers, B. Gates, Y. Yin, F. Kim, H. Yan, *Adv. Mater.* **2003**, *15*, 353.
[2] J. C. Johnson, H. J. Choi, K. R. Knutsen, R. D. Schaller, P. Yang, R. J. Saykally, *Nat. Mater.* **2002**, *1*, 106.
[3] J. C. Johnson, H. Yan, R. D. Schaller, L. H. Haber, R. J. Saykally, P. Yang, *J. Phys. Chem. B* **2001**, *105*, 11 387.
[4] M. Huang, S. Mao, H. Feick, H. Yan, Y. Wu, H. Kind, E. Weber, R. Russo, P. Yang, *Science* **2001**, *292*, 1897.
[5] P. Yang, H. Yan, S. Mao, R. Russo, J. Johnson, R. Saykally, N. Morris, J. Pham, R. He, H. J. Choi, *Adv. Funct. Mater.* **2002**, *12*, 323.
[6] J. C. Johnson, H. Yan, R. D. Schaller, P. B. Petersen, P. Yang, R. J. Saykally, *Nano Lett.* **2002**, *2*, 279.
[7] H. Kind, H. Yan, B. Messer, M. Law, P. Yang, *Adv. Mater.* **2002**, *14*, 158.
[8] M. Law, H. Kind, B. Messer, F. Kim, P. Yang, *Angew. Chem. Int. Ed.* **2002**, *41*, 2405.
[9] Z. L. Wang, *Adv. Mater.* **2003**, *15*, 432.
[10] J. Johnson, H. Yan, P. Yang, R. Saykally, *J. Phys. Chem. B* **2003**, *107*, 8816.
[11] *Fundamental of optical waveguides*, (Ed: K. Okamoto), Academic Press, San Diego, CA **2000**.
[12] H. Yan, R. He, J. Pham, P. Yang, *Adv. Mater.* **2003**, *15*, 402.
[13] Z. Pan, Z. Dia, Z. Wang, *Science* **2001**, *291*, 1947.
[14] H. Yan, R. He, J. Johnson, M. Law, R. J. Saykally, P. Yang, *J. Am. Chem. Soc.* **2003**, *125*, 4728.
[15] A. W. Snyder, J. D. Love, *Optical Waveguide Theory*, Kluwer, London **1983**, p. 243.
[16] A. V. Maslov, C. Z. Ning, *Appl. Phys. Lett.* **2003**, *83*, 1237.
[17] C. Gmachl, F. Capasso, E. E. Narimanov, J. U. Nockel, A. D. Stone, J. Faist, D. L. Sivco, A. Y. Cho, *Science* **1998**, *280*, 1556.
[18] K. Govender, D. S. Boyle, P. O'Brien, D. Binks, D. West, D. Coleman, *Adv. Mater.* **2002**, *14*, 1221.
[19] A. J. Steckl, J. C. Corelli, J. F. McDonald, in *Emerging Technologies for In-Situ Processing* (Eds: D. J. Ehrlich, V. Tran Nguyen), Kluwer, London **1988**, p. 179.
[20] I. M. Templeton, M. Fallahi, S. Charbonneau, H. G. Champion, L. B. Allard, *J. Vac. Sci. Technol. B* **1993**, *11*, 2416.
[21] S. Lipp, L. Frey, C. Lehrer, B. Frank, E. Demm, H. Ryssel, *J. Vac. Sci. Technol. B* **1996**, *14*, 3996.

Soft Solution Route to Directionally Grown ZnO Nanorod Arrays on Si Wafer; Room-Temperature Ultraviolet Laser**

By *Jin-Ho Choy*,* *Eue-Soon Jang*, *Jung-Hee Won*, *Jae-Hun Chung*, *Du-Jeon Jang*, and *Young-Woon Kim*

High-density semiconductor nanorod arrays (NRAs) with one-dimensional (1D) structures have been extensively studied for their application in photonic and electronic devices.[1,2] Especially, 1D periodic NRAs of GaN, ZnO, and ZnS have attracted considerable interest in application to ultraviolet (UV) laser devices due to their direct wide bandgaps of $\Delta E_g \geq 3.0$ eV.[1–4] Among them, ZnO ($\Delta E_g = 3.37$ eV) is thought to be the most suitable material for UV laser devices because of its large exciton binding energy of 60 meV compared to the thermal energy (26 meV) of room temperature.[5] Recently, the room-temperature UV lasing emission from a directionally grown ZnO nanoarray was demonstrated with a threshold power density below 100 kW cm^{-2}.[1,6] Such NRAs with high-quality UV lasing properties were fabricated only by physical techniques like molecular beam epitaxy (MBE), metal–organic chemical vapor deposition (MOCVD), and gold-catalyzed vapor-phase transport (VPT) techniques; those are, however, expensive and energy consuming processes since they are operated under extreme conditions.[2,7,8] For example, the high-quality ZnO NRA with the best UV-lasing properties was realized by a gold-catalyzed VPT process at 925 °C.[8] At this high temperature, however, one can hardly use a silicon (Si) wafer as a substrate, and it is necessary to

[*] Prof. J.-H. Choy, E.-S. Jang, J.-H. Won
National Nanohybrid Materials Laboratory
School of Chemistry and Molecular Engineering
Seoul National University, Seoul 151-747 (Korea)
E-mail: jhchoy@snu.ac.kr
J.-H. Chung, Prof. D.-J. Jang
School of Chemistry and Molecular Engineering
Seoul National University, Seoul 151-747 (Korea)
Prof. Y.-W. Kim
School of Materials Science and Engineering
Seoul National University, Seoul 151-744 (Korea)

[**] This work is financially supported by the Ministry of Science and Technology (NRL project) and the Ministry of Education (BK 21 program). D.-J. Jang. thanks the Strategic National R & D Program for the award of grant M1-0214-00-0108. The use of the HRTEM (JEOL, JEM-3000F apparatus) was facilitated by the Research Institute of Advanced Materials at Seoul National University.

